

Illuminating mechanochemical reactions by combining real-time fluorescence emission monitoring and periodic time-dependent density-functional calculations

Authors: Patrick A. Julien^{1*}, Mihails Arhangelskis^{1,2*}, Luzia S. Germann^{1,4}, Martin Etter³, Robert E. Dinnebier⁴, Andrew J. Morris^{5*} and Tomislav Friščić^{1*}

Affiliations:

1. Department of Chemistry, McGill University, 801 Sherbrooke St. W. H3A 0B8 Montreal, Canada; 2. Faculty of Chemistry, University of Warsaw, 1 Pasteura St. 02-093 Warsaw, Poland; 3. Deutsches-Elektronen Synchrotron (DESY), 22607 Hamburg, Germany; 4. Max-Planck Institute for Solid State Research, Heisenbergstrasse 1, D-70569 Stuttgart, Germany; 5. School of Metallurgy and Materials, University of Birmingham, Birmingham, B15 2TT, UK

Corresponding author e-mails: tomislav.friscic@mcgill.ca; m.arhangelskis@uw.edu.pl; a.j.morris.1@bham.ac.uk; patrick.julien@mail.mcgill.ca;

Abstract

We provide a proof-of-principle demonstration of the first dual-spectroscopic method for direct and real-time observation of mechanochemical reactions by ball milling, supported by high-level molecular and periodic density-functional theory (DFT) calculations, including periodic time-dependent (TD-DFT) calculations to model solid-state fluorescence spectra. By combining standard Raman and fluorescence benchtop spectrometers in a single, readily-accessible tandem monitoring technique, we simultaneously observe changes to the supramolecular structure during mechanochemical polymorph transformation and cocrystallization of the model pharmaceutical system indometacin. The observed time-resolved *in situ* spectroscopic data is supported by *ex situ* X-ray diffraction and solid-state nuclear magnetic resonance

spectroscopy measurements. The application of first principles (*ab initio*) calculations enabled the elucidation of how changes in crystalline environment, that result from mechanochemical reactions, affect vibrational and electronic excited states of molecules. The herein explored ability to interpret both real-time and *ex situ* spectroscopic data through *ab initio* calculations provides an entry into developing a detailed mechanistic understanding of mechanochemical milling processes using real-time spectroscopy.

Introduction

Mechanochemical reactions by milling, grinding, or different types of shear, have emerged as a uniquely general route to conduct the synthesis of molecules and materials without using bulk solvents.¹ The potential of mechanochemistry for making chemical synthesis more sustainable² was recognized in 2019 by International Union of Pure and Applied Chemistry (IUPAC), who placed it among the top ten emerging chemical technologies.³ Despite a wide range of existing and nascent applications, the fundamental understanding of mechanochemical reactions by milling remains limited. Time-resolved *in situ* (TRIS)⁴ monitoring based on X-ray powder diffraction⁵ (XRPD) or Raman spectroscopy⁶ has recently emerged as unrivaled approach to observe and elucidate mechanisms for a breadth of mechanochemical reactions. Currently, *in situ* XRPD approaches depend entirely on a small number of experimental setups at synchrotron radiation sources, generally limiting access to this experimental method. Monitoring based on *in situ* Raman spectroscopy is much more accessible, and capable of providing real-time information on mechanochemical reactions. However, unlike XRPD data, which can often routinely be related to detailed structural information, or even used to generate new structural understanding, the structure-based interpretation of Raman spectra of multicomponent crystalline materials is not straightforward.

Here, we present a proof-of-principle demonstration of an unprecedented integrated dual-spectroscopy approach for monitoring milling reactions in real time using readily accessible bench-top Raman and fluorescence spectrometers. This novel approach is coupled with state-of-the-art periodic time-dependent density functional theory (TD-DFT) calculations, which enables the association of spectroscopic data with the underlying molecular and extended solid-state structures of reactants and products.

To the best of our knowledge, this is the first use of visible fluorescence emission spectroscopy to follow milling transformations *in situ* and in real time. The use of fluorescence emission spectroscopy provides a so far unique possibility to detect changes in molecular structures and their solid-state environments independent of crystallinity – including the direct observation of amorphous materials. To both validate and complement this mechanochemistry monitoring approach, we integrated the fluorescence spectroscopy instrumentation with the established Raman spectroscopy monitoring setup,⁷ enabling tandem time-resolved *in situ* monitoring of milling reactions without the need for synchrotron radiation. Both Raman and fluorescence spectroscopies are non-destructive, provide simultaneous sensitivity to changes in molecular and extended solid-state structure of crystalline and amorphous solids, and can be conducted with highly accessible and low-cost setups capable of high sensitivity and acquisition speeds.⁸⁻¹¹

Besides demonstrating how this dual spectroscopy method is capable of investigating transformations of organic solids, specifically polymorphic transitions and cocrystallization, we also address an important, yet unresolved challenge in mechanistic studies of milling processes: the direct, real-time observation of amorphous material. Diverse mechanochemical transformations, from synthesizing small molecules and cocrystals,¹² to metal-organic frameworks and oxides,¹³ can be mediated by amorphous phases. In pharmaceutical materials science, ball milling is a known route to amorphous forms of active pharmaceutical ingredients (APIs), with unwanted process-induced amorphization being a major concern in materials processing and manufacture.¹⁴⁻¹⁶ Direct real-time observation of amorphous phase during milling has remained elusive due to the well-known difficulty to quantify amorphous content by XRPD without the presence of an internal and impact-resistant diffraction standard. While the recent methods for real-time *in situ* monitoring, based on either synchrotron XRPD⁵ or Raman spectroscopy,⁶ have provided unprecedented insight into kinetics and thermodynamics of mechanisms of cocrystal formation,¹⁷ the detection of amorphous content has been limited to indirect approaches based on Rietveld analysis or X-ray atomic pair distribution function data.¹⁸ ¹⁹ Here, we demonstrate that real-time Raman and fluorescence spectroscopies can directly reveal the behavior of amorphous phases during milling.

Indometacin (**ind**, Figure 1) is a versatile target for this proof-of-principle exploration of a dual-spectroscopy monitoring approach, as it provides a rich landscape of pharmaceutically-relevant, structurally well-characterized crystal forms, that are fluorescent and can undergo diverse mechanochemical transformations, including amorphization, polymorph transitions, and cocrystal formation.²⁰⁻²² Our team, and others, have previously described fluorescence²³ or Raman spectroscopy approaches to distinguish and quantify **ind** solid forms in static systems, including the amorphous form (**am-ind**); the thermodynamically more stable γ -polymorph (**γ -ind**); the metastable α -polymorph (**α -ind**), and the cocrystal of **ind** with saccharin (**sac**) (**ind-sac**).^{24,25-29} Consequently, solid **ind** was chosen as an excellent model system for this study of pharmaceutically-relevant cocrystal formation,^{12, 30,31} and amorphization^{32,33} processes by milling.

A major challenge in spectroscopic monitoring of milling reactions is the difficulty in relating spectroscopic response to structures of participating solid phases. Recently, strong changes in luminescence due to amorphization upon grinding have been reported for Pt(II)³⁴ and Au(I)³⁵ complexes, and coumarin dyes were observed to undergo an aggregation-induced blue shift in luminescence upon impact by a milling ball.^{36,37} We surmise that fluorescence spectroscopy has remained underexplored in monitoring ball milling reactions due to the difficulty in interpreting the broad emission profiles typical of organic molecules in the solid state. A possible opportunity to overcome such limitations and open spectroscopic monitoring of solids to direct and *ab initio* structural interpretation, is offered by the recent periodic density-functional theory (DFT) approaches. In principle, DFT calculations should enable the development of an integrated understanding of molecular and supramolecular transformations taking place during a mechanochemical reaction, by enabling the interpretation of spectroscopic (e.g. fluorescence, Raman, infrared, solid-state nuclear magnetic resonance – ssNMR) and XRPD monitoring data. As the first steps towards developing such integrated understanding, we now evaluate the ability of periodic and time-dependent DFT to interpret *in situ* fluorescence and Raman spectroscopy data, using calculations of ssNMR spectra as a validation benchmark. Specifically, we have used periodic DFT to assign observed Raman data to atomic motion within the crystal structure, and our recently developed method for calculating solid-state

fluorescence emission spectra of crystalline materials (using the periodic implementation of TD-DFT in the CASTEP program)³⁸ allowed us to effectively reproduce experimentally measured fluorescence spectra. At the same time, we show that the observed enhancement and wavelength shift of emission of **ind** in the solid state, compared to solution, is a result of conformational constraints imposed by the crystalline periodic environment.

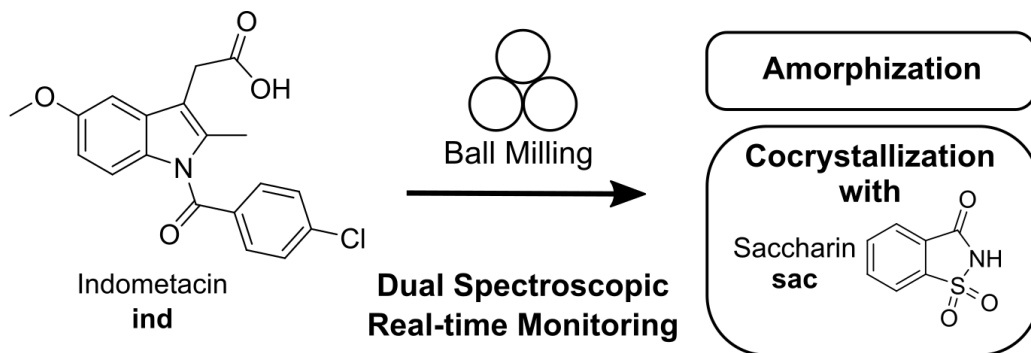


Figure 1. Model mechanochemical transformations monitored in this work using simultaneous fluorescence emission and Raman spectroscopies: amorphization and cocrystallization of indometacin (**ind**). Symbol for mechanochemical transformations adopted from Rightmire and Hanusa.³⁹

Results and Discussion

Design of the tandem spectroscopic reaction monitoring setup

We have previously highlighted **ind** as a notable example of a molecule that exhibits strong fluorescence in solid forms, but is very poorly emissive in solution.⁴⁰ Excitation and emission spectra of solid **y-ind**, **sac**, and **ind-sac** suggest an optimal excitation wavelength (λ) near 375-380 nm, with **sac** exhibiting a very weak emission and **y-ind** displaying a considerably stronger one. The emission maximum of **y-ind** is near 472 nm while **ind-sac** is slightly red-shifted to ca. 498 nm, with a higher emission intensity (Figure S5). The respective emission lifetimes for **y-ind** and **ind-sac** were measured as 1.8 ns and 5.6 ns. Bandgaps were determined from UV-Vis spectroscopic data and are statistically equivalent for both **y-ind** and **ind-sac** (Table S2). The similarity in experimental emission wavelengths, band gaps and emission lifetimes suggest similar mechanism of optical excitation and emission found in **y-ind** and **ind-sac**. The lack of fluorescence emission above 700 nm suggested the use of a 785 nm excitation laser for Raman studies without interference, enabling an effective tandem spectroscopic

approach. A fluorescence excitation source consisting of a 375 nm laser with a diverging lens to spread the excitation light, and fiber-optically-coupled spectrometer were integrated into our existing real-time Raman monitoring setup for milling reactions utilizing poly(methylmethacrylate) (PMMA) milling jars (Figure 2).⁷

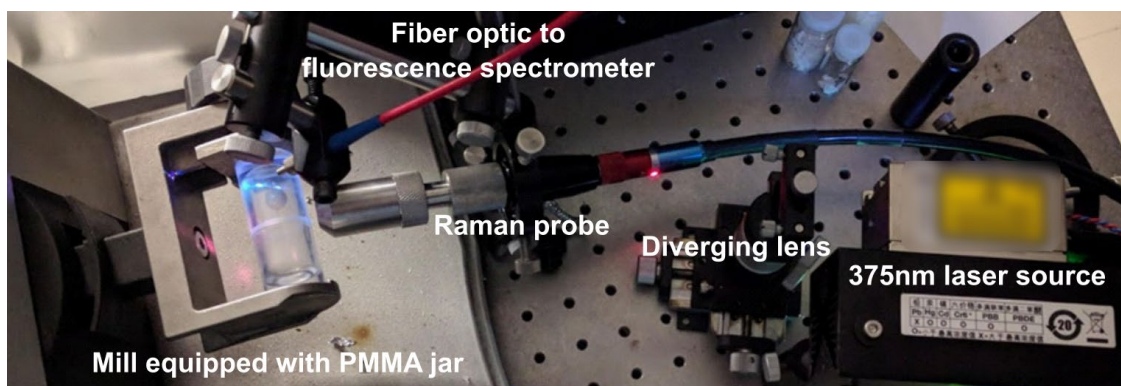


Figure 2. Instrumental setup for tandem time-resolved *in situ* monitoring of milling reactions using solid-state fluorescence emission and Raman spectroscopies.

The Raman spectra of solid **ind**, **sac**, and **ind-sac** were consistent with previous reports^{26, 27, 29} and suggest that the reaction could be monitored with minimal interference from the PMMA jar material by focusing on the 1500-1800 cm^{-1} region (Figure S12).

In situ monitoring of the cocrystallization of indometacin and saccharin

Our first target in using a tandem fluorescence and Raman spectroscopy approach to monitor a mechanochemical transformation was the cocrystallization of **ind** and **sac**, previously reported to proceed rapidly by liquid assisted grinding (LAG)²⁴ in presence of methanol (MeOH) (Figure 3a). Fluorescence spectroscopy monitoring of the milling process revealed a rapid increase in both emission intensity and a redshift of the emission maximum by approximately 30 nm to ~498 nm, consistent with the formation of **ind-sac**.²³ While the presence of MeOH could lead to the appearance of a known solvate of **ind** (CSD code BANMUZ),⁴¹ the fluorescence emission data indicated that the conversion to the cocrystal proceeds without any other solid phases, and was quantitative within 5 minutes. Completeness of conversion was verified by XRPD analysis of the product immediately after milling, revealing Bragg reflections completely consistent with the reported **ind-sac** structure (CSD UFERED),²⁴ and no trace of starting materials (Figure S2). Full conversion was also confirmed by comparing XRPD (Figure S4) and ¹³C cross-

polarization magic angle spinning (CP-MAS) ssNMR data for the milling product to a solution-made sample of **ind-sac**⁴² (Figure S20).

To verify the reaction profile indicated by fluorescence emission spectroscopy measurements, we compared the time-dependent normalized luminescence intensity at the fluorescence emission maximum with the reaction profiles determined by non-negative least squares (NNLS) fitting of both *in situ* Raman spectroscopy and fluorescence emission data. The resulting agreement (Figures 3b-g) was very good, indicating that simple monitoring of luminescence intensity can be used to directly estimate the time-dependent reaction profile over time. This provides a simple route to follow mechanochemical reactions, using a readily accessible experimental setup. Moreover, the high fluorescence intensity enables spectra acquisition rates that are considerably faster (10-500 ms) compared to either XRPD or Raman spectroscopy, and fluorescence spectroscopy is less prone to stochastic changes in intensity as fluorescence measures a larger area of the sample which is less affected by different motions of the milling assembly.⁴³ Compared to Raman spectroscopy, both fluorescence intensity measurement and the NNLS fitting profile suggest a slightly faster conversion to the **ind-sac** cocrystal, which may be a result of the difficulty in detecting low fractions of **ind** or other factors affecting fluorescence emission, such as particle size.²³ The similarity of fluorescence emission profiles between **ind** and **ind-sac** exacerbates the challenge of modeling *in situ* spectra as the sum of the spectra of pure components using the NNLS fitting method, as evidenced by patterns in the calculated residuals (Figure S17). Nevertheless, fluorescence spectroscopy provides an accessible and simple means of monitoring the kinetics of mechanochemical cocrystal formation with significant shifts in emission wavelength or intensity. The formation mechanism of **ind-sac** by LAG established by fluorescence emission spectroscopy was confirmed by separately

conducted real-time XRPD monitoring at the Deutsches Elektronen-Synchrotron (DESY) Petra III P02.1 beamline (Figures S14a,b).

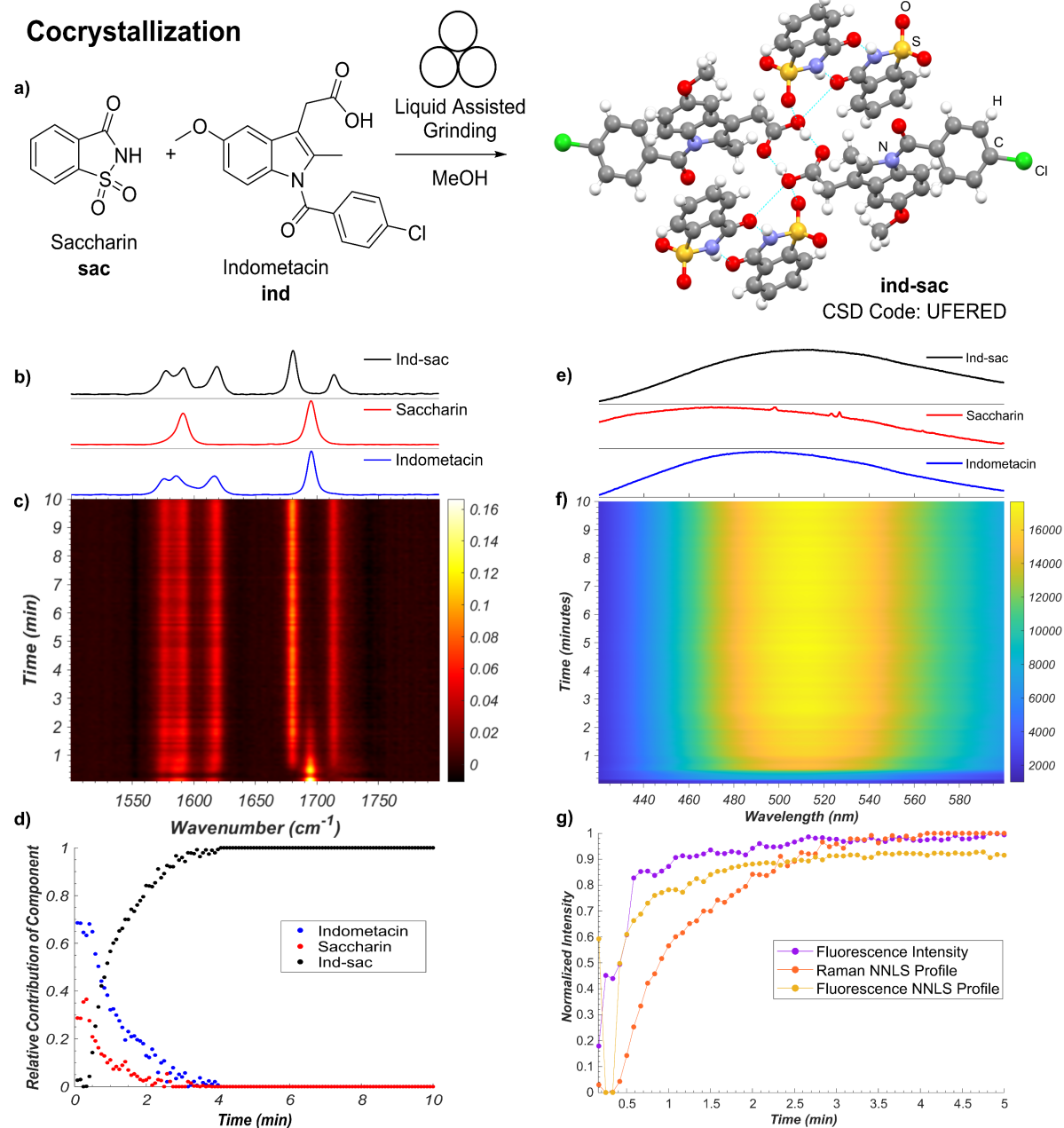


Figure 3. (a) Illustration of the monitored mechanochemical cocrystallisation of solid **ind** and **sac** upon LAG in the presence of MeOH. (b) Normalized Raman spectra of **ind**, **sac**, and **ind-sac**. (c) Time-resolved fluorescence emission acquired during the mechanochemical synthesis of **ind-sac**. (d) Relative amounts of **ind**, **sac**, and **ind-sac** estimated using non-negative least squares fitting of the *in situ* Raman dataset. (e) Normalized fluorescence emission of **ind**, **sac**, and **ind-sac**. (f) Time-resolved fluorescence emission acquired during the mechanochemical synthesis of **ind-sac**. (g) Comparison of the estimated formation of **ind-sac** via NNLS fitting of both Raman and Fluorescence data sets and normalized maximum fluorescence intensity.

Spectra interpretation using periodic DFT methods

To link the real-time spectroscopic measurements to structures of participating solid phases, we have used CASTEP plane-wave DFT calculations to simulate the Raman, infrared, and ssNMR spectra from crystal structures of **y-ind**, **sac** and **ind-sac** solids.

Periodic DFT simulations of both FTIR and Raman spectra were in good agreement with the experiment for **y-ind**, **sac**, and **ind-sac** (Figures S24-S29). While periodic DFT is required to incorporate the effects of supramolecular interactions in solid-state structures, less computationally intensive and more accessible gas-phase DFT calculations in Gaussian 16 can be used to identify and visualize key molecular vibrational modes which are experimentally observed to shift over the course of a reaction. The assignment of specific Raman bands to vibrational modes was performed for both **ind** and **sac** *via* gas phase DFT, resulting in reasonable correlation to both experimental and periodic DFT simulated spectra (Figure S34-S35). These calculations facilitated the assignment of Raman active vibrations above 1650 cm^{-1} as due to carbonyl stretching, and those between $1500\text{-}1650\text{ cm}^{-1}$ as C-C stretching of the aromatic rings in **ind** and **sac** (Figure S36-S37). In this case, the carbonyl stretches in both **y-ind** and **sac** overlap near 1695 cm^{-1} , but are observed to diverge in the **ind-sac** cocrystal. The application of periodic DFT enables the assignment of the absorption bands which shifted to higher wavenumbers (1714 cm^{-1}) as corresponding to the carbonyl stretching vibrations of **sac**, while the **ind** carbonyl stretching was found to shift to lower wavenumbers (1681 cm^{-1}) (Figure S38).

Finally, our periodic DFT model was validated by comparing the experimental ^{13}C CP-MAS ssNMR chemical shifts for all three phases with the chemical shifts calculated using GIPAW method implemented in CASTEP. Good agreement between the calculated and experimental values (Table S3, Figures S30-S32) signified the accuracy of our computational model for the crystal forms of **ind**. Notably, the most significant differences in ^{13}C chemical shifts calculated for **ind-sac** and either **sac** or **y-ind** (Table S4) were consistent with the carbon atoms adjacent to short contact interactions in the cocrystal structure, emphasizing the accuracy of the GIPAW method in quantifying the effect of supramolecular interactions on the ssNMR spectra of molecular crystals.

Understanding the solid-state fluorescence of indometacin

Beyond allowing the association of experimental data to structures of participating crystalline phases, periodic TD-DFT calculations should also enable a deeper understanding of the mechanism underlying fluorescence behavior of solid-state **ind**. Switching between solid **y-ind** and the **ind-sac** cocrystal was reported²³ to have a significant effect on emission properties of **ind**, a molecule with very low fluorescence quantum yield in solution,⁴⁰ representing an example of emission enhancement by crystal lattice effects. Previous work has shown that cocrystallization can alter optical and emission properties of organic chromophores through different mechanisms, notably forming or breaking π - π stacking interactions,⁴⁴ or by direct orbital overlap between molecules.⁴⁵

To understand the emission properties of **ind**, we turned to TD-DFT simulations of solid **y-ind** and **ind-sac**. While fluorescence emission of individual molecules can be readily simulated by TD-DFT, cubic scaling of the calculation with system size quickly makes such approach prohibitive for modelling solid-state emission by cluster expansion. As an alternative, we developed a method for simulating solid-state fluorescence emission spectra of crystalline materials using the periodic implementation of TD-DFT in CASTEP.³⁸ Since our method explicitly operates in a plane-wave basis set, it is perfectly suitable for studying the role of non-covalent interactions, orbital overlap, and conformational effects on the emission of molecular crystals. The simulated emission spectrum of **y-ind** was in excellent agreement with experiment, demonstrating the power of periodic DFT in modelling the emission behavior of crystalline solids (Figure 4). Crucially, our calculations showed excellent consistency with respect to the choice of DFT functionals: we have tested two methods for geometry optimization of electronic excited state (LDA and dispersion-corrected PBE) combined with each of the three hybrid functionals (B3LYP, HSE06 and PBE0) for single point calculation of excitation energies. All six combinations of functionals resulted in emission maxima within 0.2 eV of each other, which corresponds to 22 nm variation in λ_{max} . In terms of orbital contribution, it was found that the emission process originates from the S_1 excited state, which is dominated by the LUMO \rightarrow HOMO electron transition.

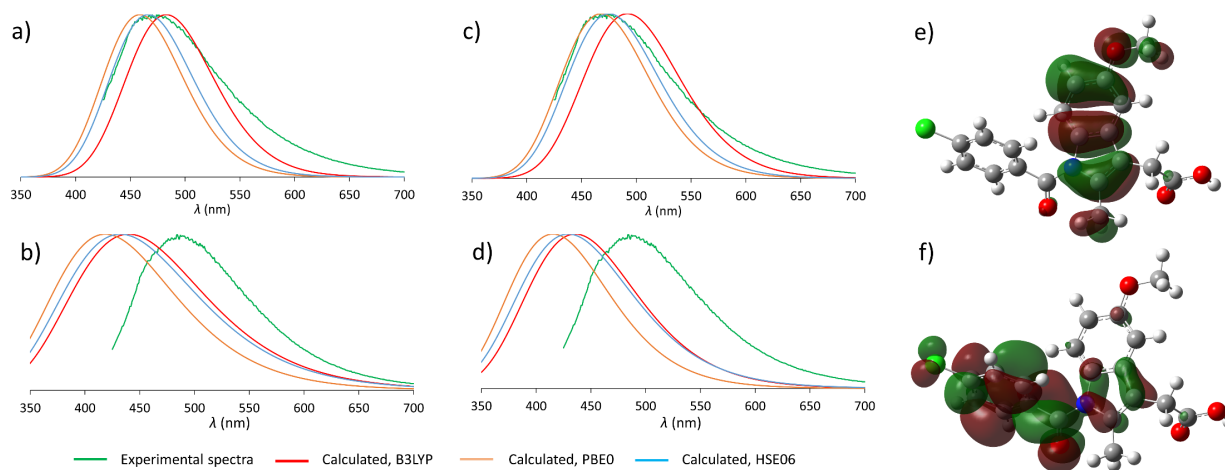


Figure 4. Comparison of the experimental (green) and simulated emission spectra. The experimental spectra are shown in green, simulated spectra are colored depending on the hybrid functional used for the single point TD-DFT calculation: red - B3LYP; orange - PBe0; blue – HSE06. a) emission spectra of **y-ind**, TD-DFT optimization with dispersion-corrected PBE; b) emission spectra of **ind-sac**, TD-DFT optimization with dispersion-corrected PBE; c) emission spectra of **y-ind**, TD-DFT optimization with LDA; d) emission spectra of **ind-sac**, TD-DFT optimization with LDA; e) HOMO orbital of an **ind** molecule, showing electron density localized on the indole fragment; f) LUMO orbital of an **ind** molecule, showing most electron density shifted towards the benzoyl moiety.

Next, we turned our attention to simulating the emission spectrum of **ind-sac** cocrystal. In cocrystals, orbital overlap between **ind** and **sac** molecules may lead to formation of electronic excited states different to those found in pure single-component crystals, therefore such a possibility had to be explored in our calculations. Through a combination of molecular and periodic DFT calculations involving hybrid and range-separated hybrid functionals we have established that fluorescence emission of the cocrystal follows the same mechanism as **y-ind**, *i.e.* transition from LUMO to HOMO of **ind**, without any significant involvement of the **sac** orbitals. Molecular TD-DFT calculations performed in Gaussian 16 with range-separated CAM-B3LYP functional convincingly ruled out the charge transfer mechanism and validated our chosen approach for periodic TD-DFT calculations (Figure 5). The calculations underestimated λ_{max} for **ind-sac** by 50-70 nm. While less accurate than obtained for **y-ind**, this presents a good level of agreement given the complexity problem of modelling solid-state emission from a multicomponent crystal.

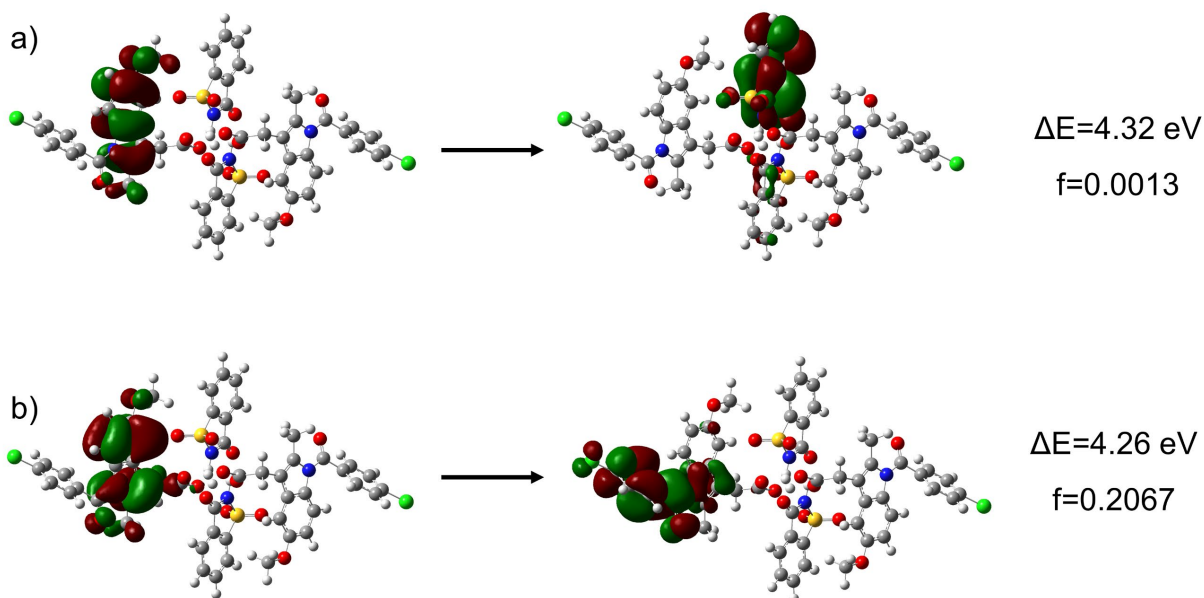


Figure 5. Molecular TD-DFT calculations using range-separated CAM-B3LYP functional on a cluster containing two **ind** and two **sac** molecules show that charge transfer state (a) has a very low oscillator strength, whereas the electronic transition localized on the **ind** molecule (b) is two orders of magnitude more intense.

An important question to be answered in the context of **ind** fluorescence is the extremely weak emission in solution, contrasting the strong emission of solid **y-ind**. The strong solvent dependence of the Stokes shift of **ind** in solution was postulated to result from a dipolar singlet excited state which is produced by intramolecular charge transfer from the indole to the benzoyl group.^{40, 46} Molecular TD-DFT calculations suggest that the electronic excitation of an isolated indometacin molecule is accompanied by a 40° rotation of the benzoyl group, such that it ends up perpendicular to the plane of the indole system (Figure 6). This can be explained by the redistribution of electron density from the indole system in the HOMO to the benzoyl group in the LUMO (Figure 4e,f). This rearrangement results in a significant reduction of the electronic transition dipole moment and therefore, quenching of the fluorescence emission. Conversely, in the crystals of **y-ind** and **ind-sac**, such rotation never exceeds 10°, regardless of the functional used for TD-DFT geometry optimization. With the phenyl group still being far from the perpendicular orientation, considerable orbital overlap between the indole and phenyl regions of the molecule provides for a higher intensity of fluorescence emission in solid-state. Evidently, the packing forces exerted by the surrounding molecules in the close-packed crystal structure

limit the geometric distortions that a molecule can undergo in the electronic excited state. The result also highlights the usefulness of our periodic TD-DFT approach to modelling solid-state fluorescence, since no such crystal lattice effects could have been detected using molecular calculations.

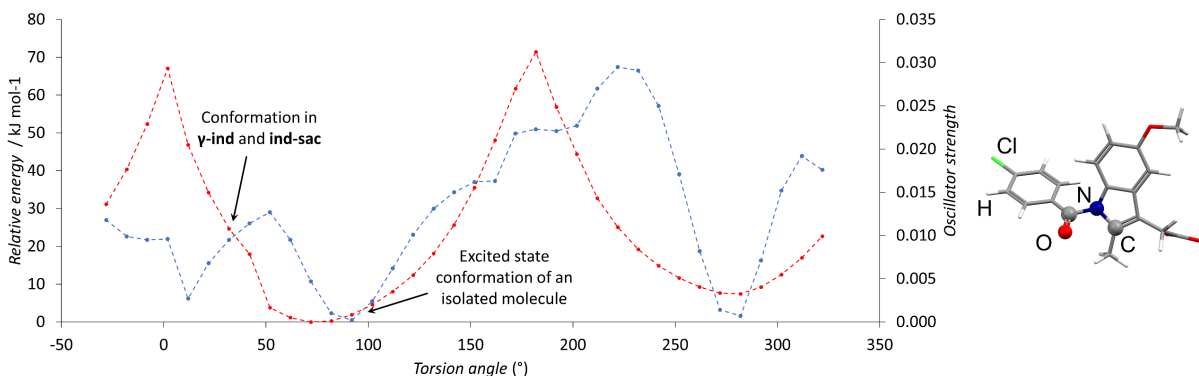


Figure 6. Calculated variation of the total energy (red) and oscillator strength (blue) for the S1 excited state of an **ind** molecule as a function of the orientation of the carbonyl group (the corresponding torsion angle is shown by the highlighted atoms in the molecular diagram). The perpendicular orientation of the benzoyl fragment found in the lowest energy conformation of the S1 state is associated with an extremely small oscillator strength, which explains low emission intensity of indometacin in solution. Conversely, the solid-state conformation is locked with the torsion angle value of $\sim 30^\circ$, where the oscillator strength is distinctly non-zero.

Milling amorphization of indometacin

Next, we applied our tandem spectroscopic monitoring method to amorphization of **ind** by neat ball milling (Figure 7a), previously explored by *ex situ* XRPD⁴⁷ and Raman spectroscopy.^{27, 28} To the best of our knowledge, this is the first report of milling amorphization of an API being monitored in real time by spectroscopy. Raman spectroscopy *in situ* monitoring of milling commercial **γ -ind** (verified by XRPD, see Figure S3) using a shaker mill operating at 30 Hz reveals the participation of at least three distinct **ind** phases: γ - and α -polymorphs (**γ - and α -ind**) along with amorphous form (**am-ind**), consistent with previously reported Raman spectra.²⁵⁻²⁹

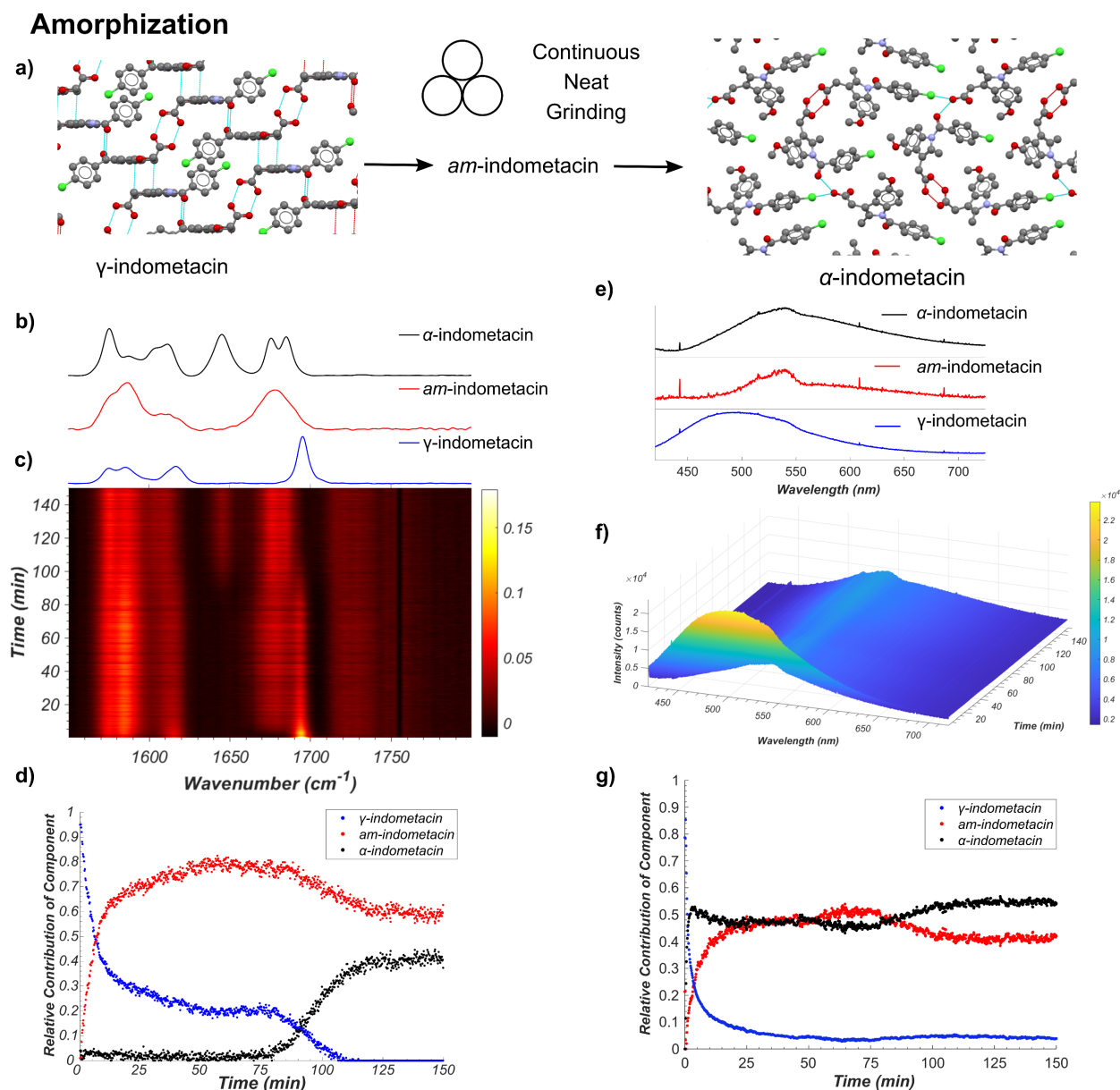


Figure 7. (a) Schematic of the monitored model transformation of neat milling solid **γ-ind**. (b) Normalized Raman spectra of **γ**-, **α**-, and amorphous **ind** synthesized via solution or melt protocols.^{48,49} (c) Time-resolved normalized Raman spectra acquired during the milling of **γ-ind**. (d) Relative amounts of **γ-ind**, **α-ind**, and **am-ind** estimated using non-negative least squares fitting of the *in situ* dataset using the reference spectra in (b). (e) Estimated fluorescence spectra of **γ-ind**, **α-ind**, and **am-ind** obtained from non-negative matrix factorization of the real time fluorescence emission spectroscopy dataset. Due to the low emission intensity of the **α**- and **am**- forms the effect of detector baseline becomes significant. (f) Time-resolved fluorescence emission data acquired during the milling of solid **ind**. (g) Relative amounts of **γ**-, **α**-, and **am-ind** estimated using non-negative matrix factorization of the *in situ* fluorescence emission dataset.

Reference spectra for all three solid **ind** phases were taken using the commercial sample of **γ-ind**, a freshly synthesized sample of **α-ind** precipitated from a solution in an ethanol/water mixture,⁴⁸ and a sample of **am-ind** made by quenching of a melt of **ind**

using liquid nitrogen.⁴⁹ Following the previously reported procedure,⁷ each measured *in situ* spectrum was fitted by a NNLS procedure using a combination of Raman spectra of pure samples to provide an estimate of the relative composition of the reaction mixture. This revealed the emergence of an amorphous phase within 10 minutes which co-exists with **γ-ind**, followed by appearance of **α-ind** after ~75 minutes. These observations are consistent with previous *ex situ* XRPD study, which suggested that milling produces a 1:1 mixture of **α-** and **am-ind**,⁴⁷ potentially in the form of **α**-form crystallites surrounded by an amorphous layer consistent with a core shell structure as previously observed for the amorphization of trehalose by milling.¹⁸ The formation of **α-ind** may be in part explained due to the glass transition of **am-ind** ($T_g = 43\text{ }^{\circ}\text{C}$),²⁶ as milling at similar conditions was previously noted to lead to temperature about $40\text{ }^{\circ}\text{C}$.⁷ As **α-** and **am-ind** exhibit fluorescence profiles similar to, and emission intensity lower than, **γ-ind** (Figure 7d), the NNLS fitting of *in situ* fluorescence data detects the initial rapid amorphization of the **γ**-form but fails to properly differentiate **α-** and **am-ind** (Figure S17c). Monitoring the maximum emission intensity of each spectrum, however, does reveal a slight increase in emission intensity corresponding to the formation of **α-ind** (S18b). The projected gradient method⁵⁰ for non-negative matrix factorization (NMF)⁵¹ was applied to simultaneously estimate both the component spectra and their associated profiles. The estimated component spectra are similar to both *ex situ* emission spectra (S18a) and resemble the reaction profile estimated by Raman spectroscopy. Accurately distinguishing the relative amounts of **α-** and **am-ind** based on fluorescence emission only remains challenging (Figure 7f), however, highlighting the complementarity inherent to the dual monitoring approach.

Analysis of solid **ind** after milling by XRPD revealed an elevated baseline and broad diffraction signals of **α-ind**, overall consistent with the presence of amorphous material (Figure S3). Attempt to characterize the sample by ¹³C CP-MAS ssNMR revealed signals identical to those for a separately synthesized sample of **α-ind** but did not reveal any amorphous content. The inability to observe **am-ind** by ssNMR suggests that the sample fully crystallized during preparation of the ssNMR experiment, which is remarkable considering the apparent steady-state behaviour of the **α-** and **am-ind** mixture during milling. While this behavior remains poorly understood, it also highlights the value of the

presented herein tandem dual spectroscopic approach for detecting mechanochemical amorphization, which is of practical importance due to the potential formation of amorphous phases during mechanical processing of pharmaceuticals and the desire to synthesize amorphous formulations of APIs to improve solubilities.⁵²

Conclusions

The utility of solid-state fluorescence emission spectroscopy in real-time monitoring of milling reactions has been demonstrated for the first time and validated using simultaneous Raman spectroscopy monitoring to yield the first dual spectroscopic approach for real-time monitoring of milling reactions. This benchtop, cost-effective tandem *in situ* monitoring technique offers an opportunity to follow and understand mechanochemical reaction mechanisms by revealing reaction kinetics and enabling the observation of amorphous phases where rapid relaxation prohibits the use of *ex situ* techniques. Such interpretation will enable the fundamental understanding and modelling of mechanochemical reactions, opening a path for rational design of solid-state reactivity. We also show that DFT calculations provide a powerful link between real-time spectroscopic measurements and structural changes in the solid state and facilitate the identification of both molecular and supramolecular reactivity. This novel combination of real-time spectroscopic measurement with DFT simulations for milling reactions shows potential to elucidate reaction mechanisms at the level of molecular and supramolecular structure, opening the door to spectroscopy-only techniques that can provide interpretable insights without the need for structural information from real-time synchrotron X-ray diffraction experiments.

Experimental

All chemicals were purchased from Sigma-Aldrich and used without further purification, including the purchased indometacin which was γ -form. Milling experiments were conducted using a RETSCH MM400 operating at 30 Hz, with a 15 mL volume PMMA milling jar and a single 3 g zirconia ball.

Milling Syntheses

The cocrystal **ind-sac** was prepared mechanochemically by milling 198 mg (0.55 mmol) **γ -ind** with 101 mg (0.55 mmol) of **sac** in the presence of 20 μ L of MeOH. Neat milling of **γ -ind** to produce **am-ind** and **α -ind** was conducted using 198 mg (0.55 mmol) **γ -ind**.

Solution syntheses

Amorphous indometacin was synthesized according to literature procedure⁴⁹ by heating 300 mg of γ -indometacin above 165 °C and pouring the resulting melt into liquid nitrogen, forming an amorphous mass which was triturated into a powder using a mortar and pestle.

α -indometacin was synthesized using a modified literature procedure⁴⁸ dissolving 300mg of γ -indometacin in 5 mL of ethanol at 80 °C before adding 10 mL of room temperature distilled water and filtering the resulting precipitate.

Fluorescence, FT-IR, XRPD, UV-Vis, Lifetimes, and SS-NMR Characterization

Preliminary fluorescence measurements were performed in clear polystyrene 96-well microplates, with sample densely packed into each well, and loaded into a Biotek Synergy 2 multi-mode microplate reader. All fluorescence lifetime measurements were conducted on a Horiba DynaMyc fluorescence lifetime mapping microscope equipped with a DeltaDiode-375L light source. Fluorescence lifetime data was fit using a single exponential function. Fourier-transform infrared attenuated total reflectance (FTIR-ATR) were measured on a Bruker Vertex 70 spectrometer with a RockSolid interferometer from 3500 cm^{-1} to 400 cm^{-1} . X-ray powder diffraction (XRPD) patterns were collected using a Bruker D2 Phaser powder diffractometer equipped with a Cu K α ($\lambda = 1.5419 \text{ \AA}$) source, nickel filter and Lynxeye detector. Ultraviolet-visible (UV-Vis) measurements were performed on a Lambda 750 UV/Vis/NIR spectrometer from Perkin-Elmer. BaSO₄ (ACS) was used as a standard for instrumental calibration (autozero correction). Samples were filled into a 1 cm^3 quartz cuvette. Full spectra were recorded in reflectance in the range of 2500-300 nm with 5 nm intervals and between 620-300 nm with 0.5 nm intervals for calculating the band gap. ¹³C Solid-state NMR spectra were collected using a Varian VNMRS 400 MHz NMR Spectrometer, with a magic angle spinning rate of 14 kHz using

a tancpx pulse sequence and calibrated with respect to the carbonyl signal of alpha-glycine signal at 176.4 ppm.

Real-time synchrotron diffraction measurements

In situ diffraction measurements were collected at the Deutsches Elektronen-Synchrotron (DESY) Petra III P02.1 beamline at an X-ray wavelength of 60 keV ($\lambda \sim 0.207 \text{ \AA}$) with a $1 \times 1 \text{ mm}^2$ collimated X-ray beam and a PerkinElmer 2D area detector operating at a time resolution of 10 seconds and a modified RETSCH MM400. All 2D XRPD patterns were integrated using Dioptas⁵³. Sequential Rietveld analysis was performed in TOPAS-Academic V5.⁵⁴ The instrumental peak profile was determined using a silicon standard measured under identical experimental conditions.⁵⁵ For visualization purposes, datasets were baseline corrected, truncated, and plotted using custom scripts in MATLAB R2018a with PMMA baseline subtraction performed using the Sonneveld and Visser algorithm.⁵⁶

***In situ* Raman Spectroscopy measurements**

All Raman spectra were collected RamanRxn1™ analyzer by Kaiser Optical Systems Inc. every 5 seconds using a 785 nm laser. Spectra were dark and intensity corrected using the Holograms® software package before being processed. Pure samples of starting materials and products were loaded on glass slides and measured. *In situ* datasets were subsequently imported into MATLAB2018a⁵⁷ and baseline corrected using the Sonneveld and Visser algorithm⁵⁶, truncated to the limits shown in the data sets, and normalized using vector normalization (L2 norm). Background subtraction of the PMMA milling jar was performed by performing a linear regression of a previously recorded PMMA spectrum to each *in situ* spectrum and subtracting the PMMA spectrum. After these corrections, the data was analyzed via NNLS, where *in situ* collected spectra were fitted as a sum of the normalized component spectra using a non-negative linear least squares algorithm (“lsqnonneg” in MATLAB) and profile estimates were normalized by setting the sum of all components in each spectrum to one.⁷

Real-time fluorescence emission spectroscopy measurements

Fluorescence measurements were conducted using a Coherent OBIS 375 nm LX 50mW excitation source and fiber-optically coupled QE65000 spectrometer from Ocean Optics. Pure samples of starting materials and products were loaded on glass slides and

measured. *In situ* datasets were subsequently truncated to the limits shown in their respective figures and plotted using custom scripts in MATLAB R2018a⁵⁷. NNLS profiles were obtained in an identical manner as described for Raman spectra. Normalized fluorescence intensity values were calculated by subtracting the minimum value of each *in situ* spectrum and dividing the spectrum by the maximum intensity value.

Periodic density-functional theory calculations of fluorescence spectra.

All periodic DFT calculations were performed in CASTEP 16.11. Calculation of solid-state fluorescence spectra of **ind** and **ind-sac** was performed using our previously described procedure.³⁸ The experimental crystal structures were converted to CASTEP input format using the program cif2cell. Initially the crystal structures were then geometry optimized in their ground state electronic configurations using either LDA functional or PBE functional combined with Grimme D2 dispersion correction. The plane-wave basis set was truncated at 750 eV cutoff combined with norm-conserving pseudopotentials, while the 1st electronic Brillouin zone was sampled with $2\pi \times 0.03 \text{ \AA}^{-1}$ k-point spacing. The crystal structures were geometry-optimized with respect to unit cell parameters and atom positions, subject to the space group symmetry constraints. Convergence was determined using the following criteria: maximum energy change: $10^{-5} \text{ eV atom}^{-1}$; maximum atomic force: 0.05 eV \AA^{-1} ; maximum atomic displacement: 10^{-3} \AA , maximum residual stress: 0.05 GPa. The optimized unit cell parameters were kept fixed through all the subsequent steps of the fluorescence calculation.

CASTEP TD-DFT calculations can only be performed at one k-point in the Brillouin zone. The k-point offering the best approximation to the converged k-point grid was selected by calculating the singlet-triplet energy difference for a series of k-points. The special k-point found to accurately reproduce the singlet-triplet energy difference for the converged k-point grid, analogous to the idea of the so-called Baldereschi point⁵⁸ was found at (1/4; -3/8; 1/8) for **γ -ind** and at (1/4; 1/8; 1/8) for **ind-sac**. Next, excited state TD-DFT calculations were performed. In the case of **γ -ind** the 1st excited state was optimized, which corresponded to the HOMO-LUMO transition on indometacin. In the case of **ind-sac**, the 1st TD-DFT excited state involved transition from HOMO(**ind**) to LUMO(**sac**), which corresponded to a low-intensity charge transfer (CT) state, known as an artefact of

TD-DFT. With the aid of molecular range-separated TD-DFT calculations (see below), this was ruled out as an incorrect solution, and instead a higher rank TD-DFT excited state corresponding to the HOMO(**ind**)-LUMO(**ind**) transition was chosen. That way both **y-ind** and **ind-sac** follow the same mechanism of phosphorescence emission.

The selected excited states were geometry-optimized using CASTEP TD-DFT module. Same input settings and convergence criteria were used here as for ground-state geometry-optimization, except for unit cell parameters which were kept fixed. The final step of the fluorescence calculation was a single point TD-DFT calculation using each of the three functionals: PBE0, B3LYP and HSE06. The hybrid calculations were performed both on the ground state- and TD-DFT-optimized geometries, the energy difference between these two geometries being used to approximate the width of the spectral line, approximated by the Gaussian curve.

Periodic DFT calculations of vibrational and NMR spectra

The ground-state optimized structures for the fluorescence calculations were used as a starting point for the Raman and NMR calculations.

For the Raman calculation the crystal structures were reoptimized with tighter a tighter atomic force convergence criterion of 0.01 eV Å⁻¹. Further, the standard and fine FFT grid scales were changed from their default values to 2 and 3, respectively. The vibrational frequencies at the Γ phonon q-point were calculated using the density-functional perturbation theory (DFPT) approach. The polarizability tensors were then calculated for the Raman-active modes. Spectra were simulated as using Gaussian functions for each Raman active vibration, using the calculated Raman frequencies, scattering activities, and a peak width of 6 cm⁻¹. All spectra were normalized to via the highest intensity for plotting.

FT-IR spectra were simulated as a summation of Gaussian functions for IR active vibrational modes using a peak width of 15 cm⁻¹, the calculated vibrational frequency, and relative peak amplitudes obtained from the CASTEP calculation. All spectra were normalized to a maximum intensity of 0.5 and converted into transmittance for comparison to experimental spectra.

The NMR parameters were calculated using the gauge including projector augmented waves (GIPAW) method. The plane-wave basis set cut-off was increased to 1000 eV, the standard and fine FFT grid scales were set to 2 and 3, respectively, and ultrasoft on-the-fly generated pseudopotentials were used.

Molecular DFT calculations

Vibrational spectra were simulated using gas phase DFT calculations run using Gaussian16W using the PBE and B3LYP functionals and the 6-311G(d,p) basis set using “tight” optimization convergence criteria. Gas phase spectra calculation and vibrational modes visualization were conducted in GaussView 6.1 using the default settings. Molecular TD-DFT calculations for an isolated **ind** molecule were performed at the CAM-B3LYP/6-311G(d,p) level of theory. The 1st electronic excited state was geometry optimized with the default convergence criteria, and then a 360° torsion angle scan in 10° steps was performed to describe the rotation of the benzoyl part of the molecule with respect to the indole fragment. The oscillator strength for the electronic transition between the 1st excited and the ground state was computed at each step of the torsion angle scan.

Acknowledgments:

This work was supported by NSERC Discovery Grant RGPIN-2017-06467; NSERC Discovery Accelerator Grant (NSERC SMFSU 507837-17) and Tier-1 Canada Research Chair Program (to TF). MA thanks the support of NCN (Poland), Sonata Grant 2018/31/D/ST5/03619. We thank WestGrid and Compute Canada for providing access to Cedar supercomputer. We are also grateful for computational support from the UK national high performance computing service, ARCHER, for which access was obtained via the UKCP consortium and funded by EPSRC grant ref EP/K013564/1. We thank McGill Chemistry Characterization Facility in the McGill University Chemistry Department for instrument use.

References

1. J.-L. Do and T. Friščić, *ACS Central Science*, 2017, **3**, 13-19.
2. K. J. Ardila-Fierro and J. G. Hernández, *ChemSusChem*, 2021, **14**, 2145-2162.

3. F. Gomollón-Bel, *Chemistry International*, 2019, **41**, 12-17.
4. G. I. Lampronti, A. A. L. Michalchuk, P. P. Mazzeo, A. M. Belenguer, J. K. M. Sanders, A. Bacchi and F. Emmerling, *Nature Communications*, 2021, **12**, 6134.
5. I. Halasz, A. Puškarić, S. A. J. Kimber, P. J. Beldon, A. M. Belenguer, F. Adams, V. Honkimäki, R. E. Dinnebier, B. Patel, W. Jones, V. Štrukil and T. Friščić, *Angewandte Chemie International Edition*, 2013, **52**, 11538-11541.
6. D. Gracin, V. Štrukil, T. Friščić, I. Halasz and K. Užarević, *Angewandte Chemie*, 2014, **126**, 6307-6311.
7. P. A. Julien, I. Malvestiti and T. Friščić, *Beilstein Journal of Organic Chemistry*, 2017, **13**, 2160-2168.
8. J. C. L. Alves and R. J. Poppi, *Analytica Chimica Acta*, 2009, **642**, 212-216.
9. A. B. Moreira, I. L. T. Dias, G. O. Neto, E. A. G. Zagatto and L. T. Kubota, *Analytica Chimica Acta*, 2004, **523**, 49-52.
10. A. B. Moreira, H. P. M. Oliveira, T. D. Z. Atvars, I. L. T. Dias, G. O. Neto, E. A. G. Zagatto and L. T. Kubota, *Analytica Chimica Acta*, 2005, **539**, 257-261.
11. S. Warnecke, Å. Rinnan, M. Allesø and S. B. Engelsen, *Applied Spectroscopy*, 2015, **69**, 323-331.
12. T. Friščić and W. Jones, *Crystal Growth & Design*, 2009, **9**, 1621-1637.
13. A. D. Katsenis, A. Puškarić, V. Štrukil, C. Mottillo, P. A. Julien, K. Užarević, M.-H. Pham, T.-O. Do, S. A. J. Kimber, P. Lazić, O. Magdysyuk, R. E. Dinnebier, I. Halasz and T. Friščić, *Nature Communications*, 2015, **6**, 6662.
14. J. F. Willart and M. Descamps, *Molecular Pharmaceutics*, 2008, **5**, 905-920.
15. V. Caron, J.-F. Willart, R. Lefort, P. Derollez, F. Danède and M. Descamps, *Carbohydrate Research*, 2011, **346**, 2622-2628.
16. M. Descamps and J. F. Willart, *Advanced Drug Delivery Reviews*, 2016, **100**, 51-66.
17. H. Kulla, S. Haferkamp, I. Akhmetova, M. Röllig, C. Maierhofer, K. Rademann and F. Emmerling, *Angewandte Chemie International Edition*, 2018, **57**, 5930-5933.
18. P. Bordet, A. Bytchkov, M. Descamps, E. Dudognon, E. Elkaïm, P. Martinetto, W. Pagnoux, A. Poulain and J.-F. Willart, *Crystal Growth & Design*, 2016, **16**, 4547-4558.
19. P. Martinetto, P. Bordet, M. Descamps, E. Dudognon, W. Pagnoux and J.-F. Willart, *Crystal Growth & Design*, 2017, **17**, 6111-6122.
20. M. Otsuka, T. Matsumoto and N. Kaneniwa, *Chemical and pharmaceutical bulletin*, 1986, **34**, 1784-1793.
21. D. Bahl and R. H. Bogner, *Pharmaceutical Research*, 2006, **23**, 2317-2325.
22. K. J. Crowley and G. Zografi, *Journal of Pharmaceutical Sciences*, 2002, **91**, 492-507.
23. M. Frenette, G. Cosa and T. Friscic, *CrystEngComm*, 2013, **15**, 5100-5106.
24. S. Basavoju, D. Boström and S. P. Velaga, *Pharmaceutical Research*, 2008, **25**, 530-541.
25. A. Heinz, M. Savolainen, T. Rades and C. J. Strachan, *European Journal of Pharmaceutical Sciences*, 2007, **32**, 182-192.

26. A. Hédoux, L. Paccou, Y. Guinet, J.-F. Willart and M. Descamps, *European Journal of Pharmaceutical Sciences*, 2009, **38**, 156-164.
27. L. S. Taylor and G. Zografi, *Pharmaceutical Research*, 1998, **15**, 755-761.
28. C. J. Strachan, T. Rades and K. C. Gordon, *Journal of Pharmacy and Pharmacology*, 2007, **59**, 261-269.
29. A. Hédoux, Y. Guinet and M. Descamps, *International Journal of Pharmaceutics*, 2011, **417**, 17-31.
30. A. Delori, T. Friscic and W. Jones, *CrystEngComm*, 2012, **14**, 2350-2362.
31. P. Vishweshwar, J. A. McMahon, J. A. Bis and M. J. Zaworotko, *Journal of Pharmaceutical Sciences*, 2006, **95**, 499-516.
32. B. C. Hancock and G. Zografi, *Journal of Pharmaceutical Sciences*, 1997, **86**, 1-12.
33. S. Hubert, S. Briancon, A. Hedoux, Y. Guinet, L. Paccou, H. Fessi and F. Puel, *International Journal of Pharmaceutics*, 2011, **420**, 76-83.
34. T. Abe, T. Itakura, N. Ikeda and K. Shinozaki, *Dalton Transactions*, 2009, 711-715.
35. H. Ito, T. Saito, N. Oshima, N. Kitamura, S. Ishizaka, Y. Hinatsu, M. Wakeshima, M. Kato, K. Tsuge and M. Sawamura, *Journal of the American Chemical Society*, 2008, **130**, 10044-10045.
36. F. P. Schafer, *Dye lasers*, Springer-Verlag, Berlin, 2nd edn., 1990.
37. E. Colacino, M. Carta, G. Pia, A. Porcheddu, P. C. Ricci and F. Delogu, *ACS Omega*, 2018, **3**, 9196-9209.
38. M. Arhangelskis, D. B. Jochym, L. Bernasconi, T. Frišćić, A. J. Morris and W. Jones, *The Journal of Physical Chemistry A*, 2018, **122**, 7514-7521.
39. N. R. Rightmire and T. P. Hanusa, *Dalton Transactions*, 2016, **45**, 2352-2362.
40. A. C. Weedon and D. F. Wong, *Journal of Photochemistry and Photobiology A: Chemistry*, 1991, **61**, 27-33.
41. S. R. B. J. G. Stowell, G. Zografi, M. Yoshioka, *CCDC 198477: Experimental Crystal Structure Determination, The Cambridge Structural Database*, 2002.
42. A. Alhalaweh, A. Sokolowski, N. Rodríguez-Hornedo and S. P. Velaga, *Crystal Growth & Design*, 2011, **11**, 3923-3929.
43. T. Frišćić, I. Halasz, P. J. Beldon, A. M. Belenguer, F. Adams, S. A. J. Kimber, V. Honkimäki and R. E. Dinnebier, *Nature Chemistry*, 2012, **5**, 66.
44. D. Yan, A. Delori, G. O. Lloyd, T. Frišćić, G. M. Day, W. Jones, J. Lu, M. Wei, D. G. Evans and X. Duan, *Angewandte Chemie International Edition*, 2011, **50**, 12483-12486.
45. J. R. G. Sander, D.-K. Bučar, R. F. Henry, J. Baltrusaitis, G. G. Z. Zhang and L. R. Macgillivray, *Journal of Pharmaceutical Sciences*, 2010, **99**, 3676-3683.
46. B. W. Disanayaka and A. C. Weedon, *Canadian Journal of Chemistry*, 1987, **65**, 245-250.
47. M. Otsuka, K. Otsuka and N. Kaneniwa, *Drug Development and Industrial Pharmacy*, 1994, **20**, 1649-1660.

48. N. Kaneniwa, M. Otsuka and T. Hayashi, *Chemical and Pharmaceutical Bulletin*, 1985, **33**, 3447-3455.
49. M. Yoshioka, B. C. Hancock and G. Zografi, *Journal of Pharmaceutical Sciences*, 1994, **83**, 1700-1705.
50. C. Lin, *Neural Computation*, 2007, **19**, 2756-2779.
51. D. D. Lee and H. S. Seung, *Nature*, 1999, **401**, 788-791.
52. B. C. Hancock and M. Parks, *Pharmaceutical Research*, 2000, **17**, 397-404.
53. C. Prescher and V. B. Prakapenka, *High Pressure Research*, 2015, **35**, 223-230.
54. A. Coelho, *Journal of Applied Crystallography*, 2018, **51**, 210-218.
55. L. S. Germann, A. D. Katsenis, I. Huskić, P. A. Julien, K. Užarević, M. Etter, O. K. Farha, T. Friščić and R. E. Dinnebier, *Crystal Growth & Design*, 2020, **20**, 49-54.
56. E. J. Sonneveld and J. W. Visser, *Journal of Applied Crystallography*, 1975, **8**, 1-7.
57. W. H. Press, S. A. Teukolsky, W. T. Vetterling and B. P. Flannery, *The art of scientific computing*, 1992, **2**, 1002.
58. A. Baldereschi, *Physical Review B*, 1973, **7**, 5212-5215.